The Astrophysical Journal, 593:946–960, 2003 August 20

IRON K LINES FROM GAMMA-RAY BURSTS

T. R. Kallman,[1] P. Mészáros,[2] and M. J. Rees[3]
Received 2001 October 24; accepted 2003 May 5

ABSTRACT

We present models for reprocessing of an intense flux of X-rays and gamma rays expected in the vicinity of gamma-ray burst sources. We consider the transfer and reprocessing of the energetic photons into observable features in the X-ray band, notably the K lines of iron. Our models are based on the assumption that the gas is sufficiently dense to allow the microphysical processes to be in a steady state, thus allowing efficient line emission with modest reprocessing mass and elemental abundances ranging from solar to moderately enriched. We show that the reprocessing is enhanced by down-Comptonization of photons whose energy would otherwise be too high to absorb in iron and that pair production can have an effect on enhancing the line production. Both "distant" reprocessors, such as supernova or wind remnants, and "nearby" reprocessors, such as outer stellar envelopes, can reproduce the observed line fluxes with Fe abundances 30–100 times above solar, depending on the incidence angle. The high incidence angles required arise naturally only in nearby models, which for plausible values can reach Fe line–to–continuum ratios close to the reported values.

Subject heading: gamma rays: bursts

1. INTRODUCTION

The discovery of iron K line emission from the afterglows of cosmic gamma-ray burst (GRB) sources provides a potentially important diagnostic of redshift as well as conditions in the burst environment. The measured line intensities, together with distance estimates, constrain the total number of iron decays needed to produce the line. A plausible assumption is that the line is formed by reprocessing of continuum photons from the burst itself or its later outflow by gas that is separate from the continuum-producing region, so that the temperature and ionization are determined by those continuum photons. If so, the time delay between the burst and the line detection provides constraints on the timescales for recombination, level decay, and light-travel time between the source of continuum source and the reprocessor. However, accurate calculations of the reprocessing of the burst continuum spectrum into lines is potentially complicated owing to the possible effects of radiative transfer, time-dependent atomic processes affecting line formation, and the gas temperature.

The statistical quality of the observations so far is not sufficient to establish a unique model that can fit the available data. A key point is that the extremely large photon fluences near a GRB are likely to be sufficient to completely ionize the nearby gas in a time that is short compared with the duration of the burst. An important criterion for evaluating any model is the reprocessing efficiency, i.e. the ratio of the iron line fluence to the continuum fluence from the burst. Under a wide range of assumptions regarding the burst continuum flux and the reprocessor density, the ionization parameter $\xi = L_{\rm inc}/nr^2$ must exceed $\sim 10^3$ (see § 2.2), where r is the distance to the source and n is the particle density. The other important observational constraint is the time at which the line emission becomes most prominent, typically several hours to a day for Fe emission features (e.g., Piro et al. 2000). This places severe constraints on the reprocessing gas and has, so far, divided the models into distinct classes distinguished by assumptions regarding the density, thickness, and composition of the reprocessing material.

In the "distant-reprocessor" scenario it is assumed that the gas illuminated by the burst and afterglow continuum is far enough for the time delay to be due to light-travel time differences. In order to achieve the required high ionization parameter, this involves reprocessing of the prompt burst emission, with luminosities of order 10^{50} ergs s^{-1}. The timescale for line emission per ion is not very short compared with the burst duration, so the reprocessing efficiencies are low if the iron abundance is solar, therefore requiring material that is highly enriched in iron in order to account for Fe line observations. Such conditions are expected to occur in models with a distant shell or ring (e.g., Weth et al. 2000; Böttcher 2000; Böttcher & Fryer 2001; Ballantyne & Ramirez-Ruiz 2001), possibly associated with supernova events (e.g., the supernova model of Vietri et al. 2001).

On the other hand, "nearby-reprocessor" scenarios are capable of much greater reprocessing efficiencies if the distances and gas densities are assumed to be comparable to those in extended stellar envelopes or in dense, thick media similar to those in the reprocessors near accreting X-ray sources. In this scenario, iron enrichment is not required and the timescales are sufficiently short that many Fe line photons are produced per Fe ion during the afterglow phase of the burst. Incident luminosities of order 10^{47} ergs s^{-1} are required at timescales comparable to a day, and radiative-transfer effects are important. Such conditions are expected, e.g., in the decaying jet model of Rees & Mészáros (2000) and in the jet+bubble model of Mészáros & Rees (2001), which differ in the origin of the nonthermal component which is reprocessed by gas at distances comparable to outer stellar envelope.

In this paper we present models that analyze these two generic families of models, with an added emphasis on the

[1] NASA Goddard Space Flight Center, Laboratory for High Energy Astrophysics, Code 665, Greenbelt, MD 20771.

[2] Department of Astronomy and Astrophysics, Pennsylvania State University, University Park, PA 16803.

[3] Institute of Astronomy, Cambridge University, Madingley Road, Cambridge CB3 0HA, UK.

case of nearby reprocessors. Our aim is to provide an understanding of the spectrum formation physics and its dependence on the physical assumptions rather than a specific model fit to the entire dynamics and light-curve histories of particular bursts. In the following sections we present in turn the physics of line formation, our modeling technique, results, and a discussion of some implications.

2. BACKGROUND

2.1. *Observations*

There are so far only a handful of observations of afterglows bright enough to allow unambiguous iron-line detections (Piro et al. 1999, 2000; Yoshida et al. 1999). Owing to the limited number of photons and to uncertainties about the source redshift and the time evolution of the line, the line flux is the best-constrained observable quantity. Comparison with models requires conversion to luminosity, which is affected by the distance estimate. As an example, we focus on the observation of GRB 991216 by Piro et al. (2000) and the distance estimate given by those authors, giving $z = 1.00 \pm 0.02$ and $D = 4.7$ Gpc for $H_0 = 75$ km s^{-1} and $q_0 = 0.5$. The maximum line luminosity was therefore $L_{\rm line} \simeq 10^{53}$ photons s^{-1} $\simeq 10^{45}$ ergs s^{-1}, with a line fluence of of $\sim 10^{49}$ ergs. As discussed by Piro et al. (2000), Lazzatti et al. (1999), Vietri et al. (2001), and others, the total mass of iron required to produce this is $\sim 50\ M_\odot/n_{\rm decays}$, where $n_{\rm decays}$ is the total number of decays per iron nucleus. This clearly demonstrates the trade-off between $n_{\rm decays}$ and the implied emitting mass of iron. If $n_{\rm decays} \gg 1$, then a moderate mass of iron is needed (e.g., Weth et al. 2000). Piro et al. (2000) also report a possible detection of a feature attributed to the recombination continuum of hydrogen-line iron, Fe XXVI. This suggests that both features are emitted by recombination in highly ionized iron.

2.2. *Ionization Equilibrium*

If the line is emitted by reprocessing of burst continuum photons, then the value $n_{\rm decays}$ cannot exceed the number of continuum photons absorbed per iron ion during the burst. This limit is achieved when both the recombination and photoionization timescales per ion are much less the duration of the burst. As an example, we adopt L_{47} as the continuum luminosity in units of 10^{47} ergs s^{-1} and R_{13} for the distance from the source to the reprocessor in units of 10^{13} cm, and we assume a power-law ionizing spectrum between 0.1 eV and 10 MeV with energy index -0.9. This is a generic index that is in the range of those observed in different afterglows in the 1–10 keV energy range relevant for Fe lines (e.g., van Paradijs, Kouveliotou, & Wijers 2000) and gives a substantial energy at $h\nu \geq 0.511$ MeV, which can contribute to pair formation. As will be seen, the pairs do not lead in the X-ray range to effects that are greatly different than in the same calculations where pair formation is artificially suppressed (Table 1). The results are less sensitive to the properties of the spectrum above a few MeV than they are to changes of the distances, densities, and so on. The recombination timescale from fully stripped into hydrogenic iron (case A) is approximately $t_{\rm rec} \simeq 7 n_{11}^{-1} T_8^{0.74}$ s, where n_{11} is the electron number density in units of 10^{11} cm^{-3} and T_8 is the electron temperature in units of 10^8 K. The photoionization timescale is $t_{\rm PI} \simeq 2 \times 10^{-7} L_{47}^{-1} R_{13}^2$ s. The preceding expression can be rewritten in terms of the ionization parameter $\xi = L/nR^2$ as $t_{\rm PI} \simeq 2 \times 10^3 \xi^{-1} n_{11}^{-1}$ s. This demonstrates that for parameter choices 10^{11} cm$^{-3} \lesssim n \lesssim 10^{17}$ cm^{-3} and $\xi \geq 10^3$ ergs cm s^{-1} the recombination timescale is greater than the photoionization timescale but that both are short compared with the burst duration ($t_{\rm burst} \sim$ 10–100 s) or the delay between the burst and afterglow, delayed jet, or bubble emergence ($t_{\rm delay} \sim 10^5$ s). Therefore the gas can be regarded as being locally in ionization equilibrium: the level of ionization will adjust itself such that the ratio of ionized (fully stripped) to nonionized (i.e., hydrogenic, helium-like, etc.) iron will be equal to $t_{\rm rec}/t_{\rm PI}$, and the value of this ratio is approximately $3 \times 10^{-3} T_8^{0.74} \xi$. This demonstrates that the gas will be highly ionized in equilibrium for ionization parameters $\xi \geq 10^3$, which, as we will show, are most plausible for GRB reprocessors.

2.3. *Assumptions*

In the remainder of this paper we focus on gas densities in this range 10^{11} cm$^{-3} \lesssim n \lesssim 10^{17}$ cm^{-3}. Such densities are comparable to those expected in massive progenitor models of GRB, e.g., in blobby "distant" shells, or in "nearby" envelope remnants illuminated by continuum from long-lasting jets or late-emerging bubbles. In addition, we assume that the temperature, ionization, and excitation conditions in the reprocessing gas are determined solely by reprocessing of continuum photons from the burst or its afterglow components. We stress that in both of these scenarios the reprocessing gas is assumed to be moving with velocities $v \ll c$, i.e., essentially at rest. That is, the reprocessing gas is physically separate from the gas responsible for the illuminating continuum photons in both models. In the "distant-reprocessor" models ($R \geq 10^{15}$ cm), either the relativistic jet producing the continuum is assumed to be inside the $v \ll c$ reprocessor shell or the geometry is such that it does not matter if it is not, and the observed $\sim 10^5$ s time lag between the burst and line detections arises from an $(r/c)(1 - \cos\theta)$ factor, where θ need not be a jet angle but may be the size of inhomogeneities in the shell (Lazzati et al. 1999; Weth et al. 2000; Piro et al. 2000; Böttcher & Fryer 2001). In the nearby-reprocessor models ($R \sim 10^{13}$ cm) the time lag of $\sim 10^5$ s arises because the outer parts of the stellar envelope (moving with $v \ll c$) are illuminated by continuum from shocks caused by a weakened but long-lived jet (Rees & Mészáros 2000) or by the late emergence of a bubble of waste heat (Mészáros & Rees 2001), in both cases at $t \sim 10^5$ s. We also assume that dynamical effects of the burst on the reprocessor are unimportant. Support for this comes from the fact that the sound crossing time for the most compact reprocessor we consider is $\geq$100 s, while the microphysical timescales are much shorter.

An added complication in comparing models with the data is the origin of the *observed* continuum in the vicinity of the line. Inherent in our models is the assumption that the line photons are emitted nearly isotropically; some anisotropy results from radiative transfer effects as the line photons escape the reprocessor, which we assume is a geometrically thin and optically thick plane-parallel slab or thin shell (although we will also discuss alternatives to this in the next section). A portion of the continuum may be observed directly and be affected by relativistic beaming, and in the vicinity of the line, this may differ from the continuum at the same energy that is incident on the reprocessor. On the other hand, the detectability of the line depends on the equivalent

TABLE 1
RESULTS FOR NEARBY MODELS 1–5 AND DISTANT MODELS 6–7

Model	n	r_{in}	ξ	μ	Fe	E_{cut}	L_{Fe26}	L_{Fe}	L_{FeUs}	Albedo	L_X	EW	L_{FeUs}/L_{ref}
1	17	13	3	1	1	6.3	44.11	44.28	42.59	0.71	45.5	0.001	−2.76
2	17	13	4	1	1	6.3	44.37	44.45	42.27	0.82	46.5	0.003	−4.14
2np	17	13	4	1	1	6.3	44.37	44.57	42.46	0.83	46.5	0.003	−3.96
2nc	17	13	4	1	1	6.3	43.15	43.40	41.73		46.7		
2′	17	13	4	0.2	1	6.3	43.95	44.18	43.6	0.97	46.5	0.048	−2.89
2″	17	13	4	0.05	1	6.3	43.1	43.6	43.7	0.97	46.5	0.014	−2.79
2 × 30	17	13	4	1	30	6.3	45.59	45.71	43.49	0.74	46.5	0.009	−2.88
2 ×100	17	13	4	1	100	6.3	45.96	46.2	43.56	0.70	46.5	0.040	−2.79
2″ × 30	17	13	4	0.05	30	6.3	43.94	44.53	44.14	0.83	46.5	0.770	−2.28
2″ × 100	17	13	4	0.05	100	6.3	44.1	44.98	44.7	0.79	46.5	1.280	−1.70
2″ × 100s	17	13	4	0.05	100	5.0	44.54	44.66	45.54	0.49	46.5	1.440	−1.65
3	17	13	5	1	1	6.3	44.77	44.99	42.34	0.90	47.5	0.001	−5.11
4	17	13	7	1	1	6.3	45.51	45.64	42.25	0.86	49.5	0.019	−7.18
5np	17	13	9	1	1	6.3	45.71	45.81	42.13	0.86	51.5	0.025	−9.30
5	17	13	9	1	1	6.3	45.69	45.79	42.11	0.87	51.5	0.025	−9.33
6	11	16	4	1	1	6.3	44.29	44.55	42.34	0.81	46.5	0.006	−4.07
6 × 1 00	11	16	4	1	100	6.3	45.81	46.44	43.51	0.70	46.5	0.011	−2.84
6 × 100 s	11	16	4	1	100	5.0	46.11	46.47	45.30	0.90	46.5	0.061	−1.15
6ni	11	16	4	1	1	6.3		44.88		0.80	46.7		
6′	11	16	4	0.2	1	6.3	43.7	44.1	43.6	0.95	46.5	0.220	−2.88
6″	11	16	4	0.05	1	6.3	42.88	44.09	43.88	0.92	46.5	0.970	−2.58
6″ × 30	11	16	4	0.05	30	6.3	43.6	45.52	45.4	0.83	46.5	1.030	−1.02
7np	11	16	9	1	1	6.3	45.91	46.04	42.27	0.87	51.5	0.020	−9.17
7	11	16	9	1	1	6.3	45.91	46.04	42.28	0.86	51.5	0.020	−9.15

NOTE.—Parameters are the reprocessor density n (cm^{-3}), distance r_{in} (cm), ionization parameter ξ (based on the incident continuum luminosity in the 13.6 eV to 13.6 keV range), $\cos\mu$ of the incidence angle relative to the surface normal, the Fe abundance in solar units, and the incident power-law cutoff in eV. In nearby models (1–5) time-delay effects are unimportant and the line luminosities L_{Fe26} and L_{Fe} correspond to H-like and total Fe, while the L_{FeUs} column is the unscattered Fe line luminosity. The last four columns are the 1–10 keV X-ray albedo, the incident X-ray luminosity, the line equivalent width in keV, and the unscattered Fe line to 1–10 keV reflected continuum ratio. All values are in the rest frame. Quantities are logarithmic, except for Fe abundances, $\cos\mu$, albedo, and equivalent width. The equivalent width is calculated as the ratio of the integrated flux in the narrow components of the iron line to the averaged interline continuum in the 6.5–7.1 keV energy range. Conversion into line emission is much less efficient for high ξ because the emission saturates at a level determined by the recombination rate, which depends primarily on n_p. For models 6 and 7 the table gives the instantaneous specific line luminosities; the observed line strengths would be reduced by a time-delay smearing factor in the integration over the large reprocessing shell. The luminosity in model 6 is typical of an afterglow after 1 day, so time smearing leads to only a modest reduction. On the other hand, the luminosity of model 7 would be relevant for the first ~10 s, and time-smearing would lead to a more significant reduction in the observed line luminosity (§ 5). The comparison models are as follows: np = no pairs, nc = no Comptonization, and ni = nickel (Fe = 0 and Ni = 20; see text). The model 6ni line luminosity is for the blend of nickel K lines; s = soft (100 keV) incident power-law cutoff.

width measured with respect to these continuum photons. The above complications are highly geometry- and model-dependent, and our goal here is to investigate what can be said about such models on the basis of a minimum of assumptions and fairly general radiation physics rather than trying to fit any particular model or observation. In what follows we present model results and discussion using the quantity that is most closely related to the physics of the reprocessor: the line luminosity. We also discuss estimates for the observed line equivalent width based on simple assumptions regarding the continuum radiation field and the reprocessor geometry.

2.4. *Line Emission*

Iron line emission in photoionized gas occurs primarily by recombination and inner shell fluorescence. The efficiency of fluorescence can be much greater than for recombination, but the ionization conditions required are less likely to be applicable to GRB reprocessors.

The efficiency of line emission by recombination is given by the product of the effective Fe XXVI Lyα recombination rate coefficient and the emission measure ionized by the burst continuum. This quantity can be approximated as

$$\frac{L_{rec}}{L_{inc}} \simeq \frac{4\pi N \alpha \epsilon y_{Fe} x_{Fe\,XXVII}}{\xi} , \quad (1)$$

where L_{rec} is the line luminosity, L_{inc} is the incident ionizing continuum luminosity, N is the radial column density of the shell, $\alpha \simeq 3.4 \times 10^{-13}$ cm^3 s^{-1} is the effective recombination rate coefficient for production of the line, ϵ_{line} is the line energy, $x_{Fe\,XXVII}$ is the ionization fraction of fully stripped iron, y_{Fe} is the iron abundance, and $\xi = L/nR^2$ is the ionization parameter (e.g., Tarter, Tucker, & Salpeter 1969). This quantity is the ratio of the line luminosity radiated by an optically thin spherical shell to the luminosity of the central exciting source, and it enters the equation because the recombination emission rate is proportional to gas density. Inserting plausible numerical values gives

$$\frac{L_{rec}}{L_{inc}} \sim \frac{1.4 N_{24} y_{\odot} x_{Fe\,XXVII}}{\xi} , \quad (2)$$

where N_{24} is the column in units of 10^{24} cm^{-2}. The fractional abundance of highly ionized iron is negligible for ionization parameters $\xi \leq 10^3$ ergs cm s^{-1}, so the maximum fractional recombination luminosity attainable is $\sim 10^{-3}$.

Inner shell fluorescence can occur if iron is not highly ionized, i.e., if the typical ion has three or more bound electrons. The luminosity is

$$\frac{L_{\rm fl}}{L_{\rm inc}} \simeq \omega_{\rm fl} N \sigma_{\rm PI} f_\epsilon \frac{\Delta\epsilon}{\epsilon} \epsilon_{\rm line} y_{\rm Fe}\, x_{\le {\rm Fe\,XXIV}} \ , \tag{3}$$

where $\omega_{\rm fl}$ is the fluorescence yield (0.34 for neutral iron), $\sigma_{\rm PI}$ is the photoionization cross section at threshold, f_ϵ is the normalized spectral function at the K threshold energy (see Kallman & McCray 1980 for a definition), $\Delta\epsilon/\epsilon$ is a number of order unity that describes the fractional energy bandwidth contributing to the photoionization rate integral [for a power law with energy index α one has $\Delta\epsilon/\epsilon = 1/(3+\alpha)$], and $x_{\le {\rm Fe\,XXIV}}$ is the ionization fraction of all iron ions with three or more electrons. The rate for fluorescent line emission is proportional to the ionizing flux, so the efficiency is independent of ξ. Inserting plausible numbers gives

$$\frac{L_{\rm fl}}{L_{\rm inc}} \sim 0.005 N_{24} y_\odot x_{\le {\rm Fe\,XXIV}} \tag{4}$$

for a single power-law spectrum with an energy index of -0.9.

Another convenient measurement of line strength is the equivalent width measured with respect to the continuum incident on the reprocessor, given by

$${\rm EW} = \frac{L_{\rm line}}{L_{\rm inc} f_\epsilon} \simeq \frac{L_{\rm line}}{L_{\rm inc}} \epsilon_{\rm line} \kappa \ , \tag{5}$$

where κ is a numerical factor depending on the shape of the incident continuum, $\kappa = \ln(E_{\rm max}/E_{\rm min}) \simeq 7$ for our choice of power law with energy index -1 and where the continuum luminosity is measured between 13.6 eV and 13.6 keV. This shows that fluorescence lines can have equivalent widths of $\sim$1 keV or fractional luminosities of $\sim 10^{-2}$ but that they require low-ionization parameter $\xi \le 10^3$ ergs cm s^{-1}.

For burst luminosities in the range 10^{47}–10^{52} ergs s^{-1} and distances $\le 10^{15}$ cm from the source, gas densities $\ge 10^{15} \xi_3^{-1} L_{48} R_{15}^{-2}$ are implied if $\xi \le 10^3$. This is at the limit of what we consider in the models that follow. So, although fluorescence is included in all our models, it turns out to be generally less important than recombination, and the model equivalent widths (defined as in eq. [5]) are less than the maximum attainable.

3. COMPUTATIONAL TECHNIQUE

More accurate treatments of gamma-ray reprocessing and iron line emission require calculations of the ionization balance and electron kinetic temperature in the gas, along with the emission measure of gas that can emit lines. Calculation of ionization balance and temperature is straightforward given the local mean intensity of ionizing photons; calculating the transfer of these photons is complicated owing to scattering and attenuation by Compton scattering and photoelectric absorption. Compton scattering can redistribute photons from high energies ($\gtrsim$1 MeV) to energies where photoelectric absorption is important and absorption depends on the local ionization balance. In addition, high-energy photons can produce e^+e^- pairs by collision with lower energy reprocessed photons, and these pairs can affect the ionization balance of iron by contributing to recombination, as well as contributing to Compton scattering of continuum photons. An accurate treatment of all these process requires a numerical solution.

The problem of reprocessing of gamma rays and hard X-rays and iron-line formation does not lend itself easily to most of the numerical techniques developed for treating either photoionized reprocessing or Comptonization. This is because Compton scattering is likely to be important if the column density of the reprocessor is large (e.g., $\ge 10^{24}$ cm^{-2}) and because the scattering must be treated relativistically in order to accurately treat the gamma rays with energies $\gtrsim$1 MeV. Models developed for iron line formation in active galactic nuclei accretion disks (see, e.g., Nayakshin et al. 2000; Ballantyne, Ross, & Fabian 2001) that utilize Fokker-Planck or convolution methods for Comptonization are not highly accurate if these gamma rays are important. At the same time, the reprocessing gas temperature must be $\sim 10^8$ K or less, owing to limits on broadening of the observed lines, so that models developed for relativistic plasmas (e.g., Coppi & Blandford 1990) are also not directly applicable.

The reprocessing of gamma rays can affect the iron K line production in two ways. First, down-Comptonization in a gas with mean electron energy that is small compared with the gamma-ray energy will soften the spectrum in the interior of the reprocessor. This can enhance the production of line photons owing to the increase in the cross section for iron photoionization at low energies. In addition, incident gamma rays at energies greater than $\sim$1 MeV can produce pairs by γ-γ collisions with reflected photons if the center of mass energy is greater than the threshold for this process. This can enhance the rate of recombination onto iron and can change the mean free path for Compton scattering.

The models presented here make use of the Monte Carlo technique for treating the transfer of continuum photons. This has the advantages that it allows for exact treatment of the relativistic rates and cross sections for Compton scattering and photon destruction and that pair production can be incorporated in a straightforward way. We use the Monte Carlo code as described in Hua (1997), with modifications to allow for photoabsorption and pair production.

In order to calculate line formation and photoelectric absorption, it is necessary to combine the photon flux derived from the Monte Carlo calculation with a calculation of the heating, ionization, and excitation of the gas. To do so we use a photoionization equilibrium model (XSTAR; Kallman & Bautista 2000; Bautista & Kallman 2001), using the ionizing flux from the Monte Carlo calculation at each point in the cloud. This calculation is iteratively repeated 3–5 times in order to self-consistently account for photoelectric absorption and Compton scattering. Transfer of the line photons and thermal continuum photons escaping the cloud is calculated using the XSTAR escape probability formalism to calculate the local escaping flux, and then Comptonization of the line is calculated using an additional Monte Carlo step.

Input parameters are ionization parameter ξ, the continuum spectral shape (which we take to be single power law with energy index -0.9 from 0.1 eV to 10 MeV), gas density, and elemental composition. The spectral index is chosen to be constant over the entire spectrum for simplicity and because this value is representative of the observations in the 1–10 keV energy band. Any departures from this value at energies below 1–2 keV, which may be caused by absorption in the host or our own galaxy, are unimportant for the

purposes of modeling the iron K lines. It is conventional (e.g., Krolik, McKee, & Tarter 1981; Kallman & Bautista 2000) to define the ionization parameter in terms of the incident energy flux of photons integrated from 13.6 eV to 13.6 keV and the gas (nucleus) number density $\xi = 4\pi F/n$, where $F = \int_{13.6\mathrm{eV}}^{13.6\mathrm{keV}} F d\epsilon$. The total incident photon number flux is $F_{\mathrm{inc}}^{(n)} = \int_0^\infty F_\epsilon/\epsilon d\epsilon$. The chemical composition should be model- and assumption-dependent; hence, in general a conventional (solar) choice is used,

$$[\mathrm{H} : \mathrm{He} : \mathrm{C} : \mathrm{O} : \mathrm{Ne} : \mathrm{Si} : \mathrm{S} : \mathrm{Fe}] = [12 : 11 : 8.65 : 8.87 : 8.14 : 7.57 : 7.28 : 7.50]$$

(Morrison & McCammon 1983). In Table 1 and § 6 we explore the effect of departures from solar abundances.

We perform the Monte Carlo transfer calculation for a total number of photons N_{tot} (100 photons per energy bin for each of 500 bins) to get the number distribution of photons versus depth and energy $N(\epsilon, z)$. At each scattering the cross sections for Compton scattering (fully relativistic in both photon and electron energy), photoelectric absorption, and pair production (described in more detail in the following section) are calculated. The fate of the photon is determined by calculating the path length for each process, including escape, and taking the smallest. Then the number distribution of photons versus depth and energy is converted to a local energy flux using $F_{\mathrm{local}}(\epsilon, z) = F_{\mathrm{inc}}^{(n)} N(\epsilon, z)/N_{\mathrm{tot}}$. This then used to calculate the ionization balance and temperature throughout the slab using XSTAR. Compton heating and cooling is calculated fully relativistically using the results of Guilbert (1986). Both Monte Carlo and photoionization steps are repeated a number of times (∼4) to self-consistently calculate transfer, ionization, pair production/annihilation, and so on.

4. MODEL RESULTS

4.1. *Input and Output Parameters*

The key issues we wish to address with these models are the following:

1. What is the penetration of the gamma rays and X-rays into the reprocessor, and how important is the down-Comptonization of gamma rays?
2. What is the albedo of the reprocessor to gamma rays, and what is the spectrum of the reflected gammas?
3. What is the efficiency of iron line emission, and does it scale with ξ as predicted by equations (2) and (4)?

To address these issues, we have run the models summarized in Table 1. These span a range of values for ionization parameter and include models designed to test some of the assumptions described so far. The reprocessor distance range is 10^{13}–10^{16} cm, the gas densities are 10^{11}–10^{17} cm^{-3}, and the incident continuum luminosity range is 10^{46}–10^{52} ergs s^{-1}. The smaller distance is comparable to a massive stellar envelope, while the densities range from those that might be encountered in clumpy blobs of a $\sim 1\ M_\odot$ shell at a light-day distance, up to typical atmospheric or clumpy ejecta densities at massive stellar envelope distances. The high values of incident luminosity L_{inc} are characteristic of the earlier epochs (minutes), while the lower ones are characteristic of later epochs (several hours to days). The ionizing spectrum is held constant throughout. We have also explored the dependence of models on the iron abundance, on the angle of incidence on the model slab, and on computational assumptions such as the treatment of pairs and Comptonization.

Table 1 presents the results of our model calculation: ionization parameter and iron line strength, Fe XXVI Lyα alone (in the column labeled L_{Fe26}), and total Fe K in the 6.4–6.9 keV range (in the column labeled L_{Fe}). These line luminosities correspond to the total emitted line luminosity without attempting to distinguish the un-Comptonized fraction. Of more interest are the observable quantities—the line luminosities that escape unscattered and their strength relative to the continuum. Table 1 lists the luminosity of the iron line that escapes unscattered, L_{FeUs}, and two different measures of the line reprocessing efficiency—the ratio of the unscattered line to the reflected continuum luminosity, $L_{\mathrm{FeUs}}/L_{\mathrm{ref}}$ and the equivalent width. For our purposes, the reflected luminosity is integrated over the 1–10 keV energy band and calculated according to $L_{\mathrm{ref}} = \mathrm{albedo} \times L_{\mathrm{X}}$, and both the albedo and L_{X} are given in the table. The equivalent width is calculated as the ratio of the integrated residual flux in the unscattered components of the iron line to the averaged interline continuum in the 6.5–7.1 keV energy range. These quantities are all calculated in the source rest frame.

4.2. *Total Emitted Line Luminosity*

In Figure 1 we plot the line luminosities from Table 1 as a function of ionization parameter for the nearby models. This shows the behavior predicted by equations (1) and (2), i.e., that the line reprocessing efficiency decreases approximately inversely with increasing ionization parameter. For the distant models at $R = 10^{16}$ cm, we find that the $L_{\mathrm{line}}/L_{\mathrm{inc}} \propto \xi^{-0.75}$. Comparison of equation (2) with the line formation efficiencies derived from the total line luminosities in the table shows a difference of a factor of ∼10–50. This is due to the influence of Comptonization, which increases the flux of photons available to ionize iron and hence the line-emitting volume. A further illustration is provided by the results of model 2nc, which was calculated with the same parameters as model 2 but using simple single-stream exponential attenuation of the incident photons rather than the Monte Carlo Comptonization calculation. The efficiency of model 2nc is very nearly the same as that predicted by equation (2).

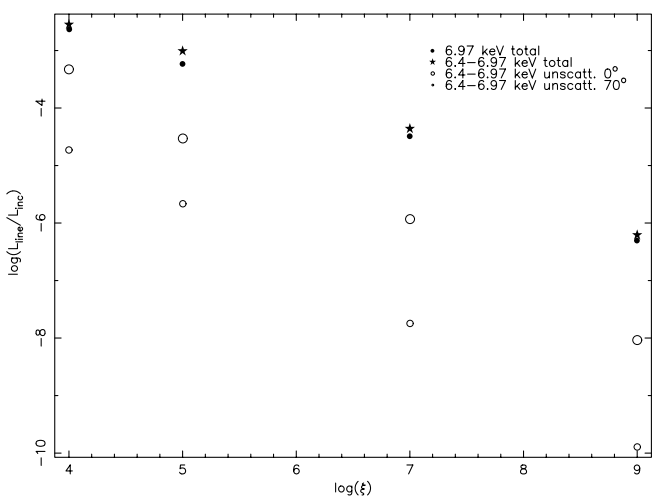

FIG. 1.—Line reprocessing efficiency vs. ionization parameter for the nearby models shown in the table.

Question 1 can be addressed by comparing models 2 and 2nc. The effect of an accurate transfer treatment is to allow penetration of gamma rays due to the enhanced forward-scattering probability of the Klein-Nishina (KN) cross section and also to allow down-Comptonization of these penetrating photons at large column depths in the slab. For the estimates in the previous section we took $\tau_{\rm Th} \simeq 1$ for the Thompson depth of the ionized part of the slab, but the Monte Carlo results show that photons penetrate to much greater depths. In Figure 2*a* we show a contour plot of photon intensity versus energy and depth for model 2, which shows that the incident radiation field is not depleted until $\tau_{\rm Th} \simeq 10$. This accounts for the greater line intensity in model 2 than in model 2nc.

Figures 2*a*–2*c* give more details of the spatial distributions of various physical quantities in model 2 for normal incidence. Figure 2*a* shows a contour plot of the ratio of photon mean intensity in the interior of the model to that at the surface as a function of energy and optical depth. The contour spacing is a factor of 1.6 in this figure, and dashed or solid contours indicate regions where the ratio is less than or greater than unity, respectively. This shows that photons below $\sim$100 keV penetrate to $\tau_{\rm Th} \sim 10$ for this choice of parameters before the intensity falls below 0.1 of the surface value. The mean intensity increases with increasing depth to a maximum at $\tau_{\rm Th} \simeq 3$. The flux would be zero in a pure scattering slab, but the effects of photoabsorption and reemission, which shifts photons into the UV, results in a nonzero net flux. Figure 2*b* shows the electron temperature versus depth. Near the surface the gas approaches the Compton temperature, $T_{\rm IC}$, which in this case is $\simeq 3 \times 10^8$ K. The blip near 10^5 K is a common feature in thermal equilibrium curves, being related to nonlinearities in the heating and cooling from intermediate-mass elements such as oxygen. Collisional cooling has a temperature dependence $\exp(-\text{const}/T)/\sqrt{(T)}$, and the local maxima in this

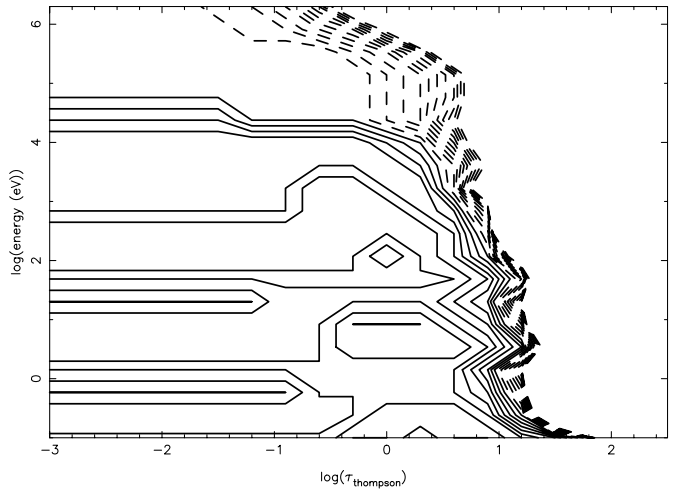

FIG. 2*a*

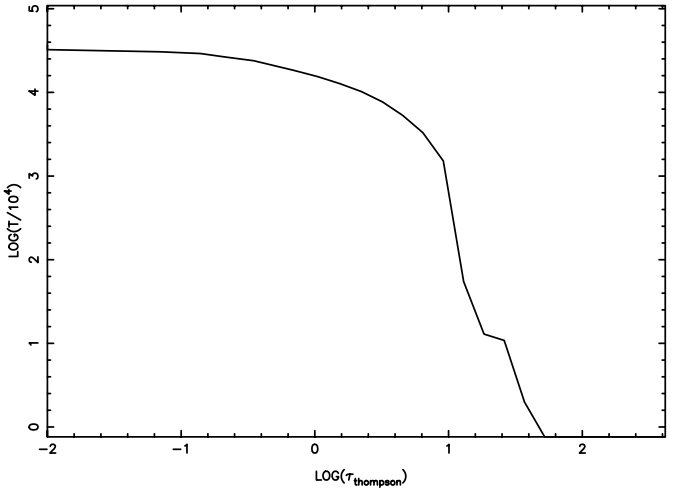

FIG. 2*b*

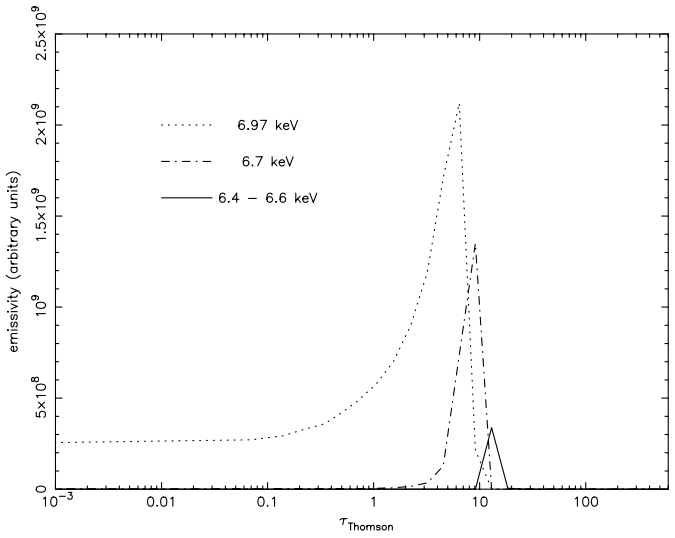

FIG. 2*c*

FIG. 2.—(*a*) Contours of constant mean intensity relative to the incident intensity vs. energy and Thomson optical depth for model 2. Contours interval is 0.2 dex. Solid contours correspond to mean intensity greater than incident and demonstrate the effects of Compton down-scattering. Dashed contours correspond to mean intensity less than incident and demonstrate the effects of attenuation and Compton reflection. (*b*) Temperature vs. depth for model 2. (*c*) Iron line emissivity vs. depth for model 2 for the various components: 6.97 keV (hydrogen-like iron), 6.7 keV (He-like iron), and 6.4–6.6 keV (all lower stages).

function can lead to such bumps. Figure 2*c* shows the distribution of emissivity with depth in model 2. The various curves correspond to the components of the iron line from the hydrogen-like (*dotted contours*), helium-like (*dot-dashed contours*), and lower (*dashed contours*) ion stages. This reflects the dominance of recombination onto hydrogen-like iron in this model, owing to its large ionization parameter.

4.3. *The Effects of Comptonization on the Line-escaping Spectrum*

The mean wavelength shift for iron K line photons per Compton scattering in the hot, ionized part of the reprocessor is $\Delta\epsilon \simeq 0.46$ keV. This is sufficient to smear line photons beyond recognition, so as a practical matter we expect that only unscattered photons will be recognizable as being associated with a line. We have modeled the effects of Comptonization on the line and thermally emitted continuum photons created in the models using the procedure described in the previous section. Figure 3*a* shows the spectrum in the 5–10 keV energy band for model 2 at normal incidence. The dashed curve shows the total emitted spectrum integrated over the slab, including the Lyman series lines and Lyman continuum emission of Fe XXVI and the 1–*n* lines and recombination emission of Fe XXX. This model also emits Lyman lines and recombination continua from O VIII and lines from highly ionized Si and S (not shown). The lowest of the solid curves shows the Comptonized line and thermally emitted continuum spectrum escaping the cloud, calculated self-consistently using a Monte Carlo treatment. Statistical uncertainties associated with the Monte Carlo treatment of scattering in this figure are small; we emit 1000 photons in each of the energy bins in our model; the few apparent gaps in the injected spectrum are due to slight mismatches in mapping between the energy grids used for the Monte Carlo and the XSTAR part of the calculation. For the purpose of treating the line escape from the cloud, we have added the process of line-resonant scattering to the Monte Carlo calculation, so that we account for the enhancement to the photon path length and the probability of Compton scattering for resonance-line photons such as Fe XXVI Lyα. In doing so, we assume that each line-scattering event is treated according to complete redistribution in the line Doppler core and is completely coherent in the line wings. In practice, the latter is unimportant, since Fe XXVI Lyα has maximum depth of $\sim$1000, and the damping parameter is $\simeq 10^{-4}$. The results of the calculation of the luminosity in the unscattered core of the Fe XXVI Lyα line, for all our models, is also given in the column of the Table labeled $L_{\rm FeUs}$. The upper solid curve, plotted with coarser binning, is the reflected Comptonized continuum for this model.

The results of Figure 3*a* for normal incidence show that the fraction of the line photons escaping unscattered is $\sim$0.01; most of the luminosity escapes as a broad Comptonized continuum in the vicinity of the line. The narrow core of the 6.97 keV line has an equivalent width EW $\simeq$ 3 eV and a fractional luminosity $L_{\rm FeUs}/L_{\rm ref} \simeq 7.2 \times 10^{-5}$, measured relative to the total scattered flux integrated over the 1–10 keV energy band. This figure, as well as Figure 2*c*, shows that although various components of the line are emitted, the components at energies 6.7 keV (He-like) and below are more Comptonized than the component at 6.97 keV (H-like). This is because the higher energy (H-like) component

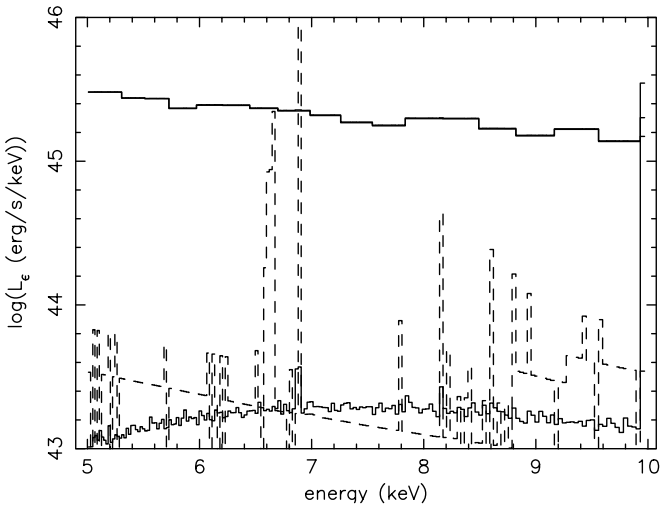

FIG. 3*a*

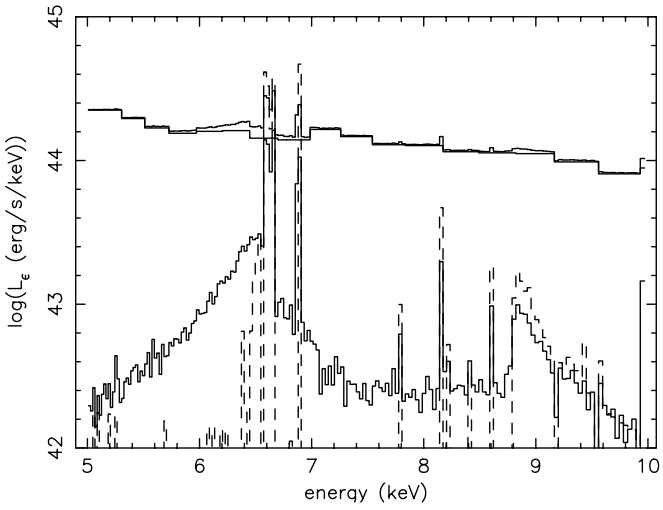

FIG. 3*b*

FIG. 3.—Reflected (*solid curves*) and emitted (*dashed curves*) rest-frame spectra from nearby models with solar abundance of iron, varying the incidence angle. Units are specific luminosity, corresponding to the reflected and reprocessed spectrum from gas surrounding a source with ionizing luminosity 10^{47} ergs s^{-1}. Solid curves correspond to Comptonized thermal emission, Compton reflected continuum, and total. (*a*) Model 2 with normal incidence. (*b*) Model 2′′ with nonnormal incidence ($\mu = 0.05$).

is emitted in the shallower, more highly ionized gas closer to the slab boundary and therefore traverses a smaller depth as it escapes. The recombination continua are apparent in the emitted spectrum but are unrecognizable in the scattered escaping spectrum. Resonance scattering does not affect the photons emitted in the higher Lyman series lines or the recombination continuum as much as the Lyα line, so the ratio of these lines to the Lyα analog line exceeds the recombination value in our simulations.

The difference in the luminosity escaping unscattered and the emitted luminosity is displayed for all models in Table 1 and is plotted in Figure 1 for the nearby models. This shows that the effects of Comptonization of the escaping line are greater at high ξ. This is due to the relative importance of scattering and photoelectric absorption as a function of ionization parameter. At high ξ, photoelectric absorption is reduced in importance, so that incident photons penetrate

to greater Compton depths before being absorbed and reemitted as iron-line photons.

The effects of Comptonization on the escaping line profile are reduced if the line resonance scattering optical depth scale is changed. This might occur if, for example, the cloud had a large internal velocity dispersion of $\sim$3000 km s^{-1}. Numerical experiments show that this affects the unscattered line luminosity by a factor of $\leq$2, reflecting the fact that the regions of large line depth are also regions of large continuum Thomson depth, and photons emitted in these regions are likely to be Comptonized even if they escape without resonance scattering.

4.4. *Incidence Angle and Abundance Dependence of the Lines*

The depth scale for scattering of all photons is affected if the incident photons hit the slab at a nonnormal angle. The effects of this are displayed in Table 1 and Figures 1 and 3*b*. As shown in Table 1 and Figure 1, if the incident angle is 70° ($\mu = 0.2$), then the unscattered line luminosity is increased by a factor of 10–30 compared with normal incidence. If the incident angle is increased to 87° ($\mu = 0.05$), then the effects of Comptonization on the luminosity of the narrow-line core are negligible; the escaping unscattered line luminosity is comparable to the total emitted.

This is illustrated in Figure 3*b* for model 2″, which has an incidence angle of 87°, for comparison with the normal incidence case of model 2 in Figure 3*a*. Also notable in this figure is the fact that the fraction of the unscattered He-like line near 6.7 keV is greater than for the H-like line at 6.97 keV. This is significantly different from the results for normal incidence, for which the unscattered fraction of the He-like line is negligible. This is due to the differing scattering behaviors of the two lines: the H-like line is subject to resonance scattering, while the forbidden and intercombination components of the He-like line are not, but the H-like line is emitted closer to the illuminated surface. At normal incidence the disparity in depths of emission is more important than the difference between resonance and nonresonance scattering, while at 87° the converse is true. The net effect of nonnormal incidence is to reduce the Thomson depth of the hot ($\sim 10^8$ K) scattering layer of the model clouds. Evidence for this in the results of model 2″ and other nonnormal incidence models is the "shoulder" below the 6.7 keV line in the scattered spectrum. This is because in all models a significant fraction of the 6.4–6.7 keV line photons penetrate into the cold part of the cloud and scatter there. In this region the Compton energy shift per scattering is always to lower energies, $\simeq$0.08 keV, thus reducing a low-energy shoulder on the line. In the nonnormal incidence models many of these photons escape owing to the reduced optical depth of the hot cloud layer. Although this shoulder is narrow enough that it might be interpreted as being part of the line by low-resolution instruments, we do not include it in our accounting for escaping unscattered photons. We do include it in the continuum accounting, and this affects the equivalent widths we derive, as discussed in the following section.

In most of our models the iron line emission is dominated by recombination, so that the total line luminosity is expected to scale with the increase in the iron abundance, and at least for the nearby reprocessors, this scaling is geometry independent. An increased iron abundance results in enhanced cooling and lower equilibrium temperature, which in turn increases the recombination rate coefficient, and the penetration and escape depth are also affected in a nonlinear manner. We have carried out experiments using model 1, the lowest ionization parameter case, indicating that the total emitted iron luminosity scales approximately as the square root of the iron overabundance for enhancements of up to a factor of $\sim 10^2$ over solar values. The escaping unscattered component of the Fe XXVI Lyα line scales somewhat more slowly with the abundance because of resonance-line trapping; e.g., for normal incidence reprocessing the unscattered line scaling with abundance is $d \log \left(L_{\rm Fe}^{\rm (us)}\right)/d \log({\rm Fe\ abundance}) \sim 0.4$.

For two models chosen as representative of the nearby and distant cases, models 2 and 6, we have performed calculations where the Fe abundance is 30 and 100 times the solar value. Figure 4 show the results for two nearby models, model 2″ × 30 (85° incidence angle with Fe 30 times solar;

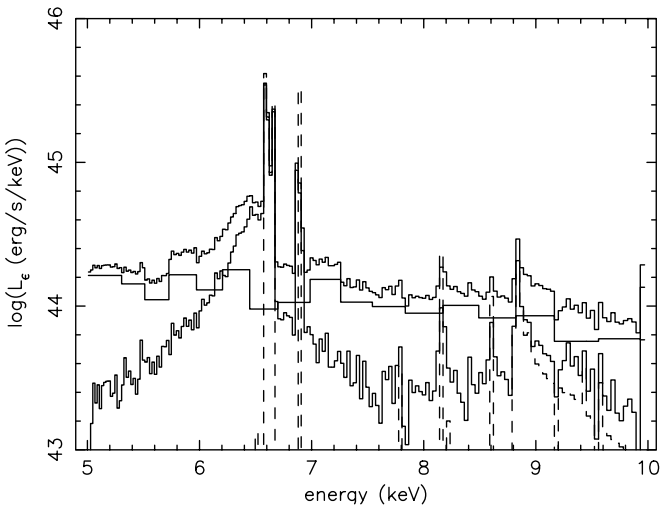

FIG. 4*a*

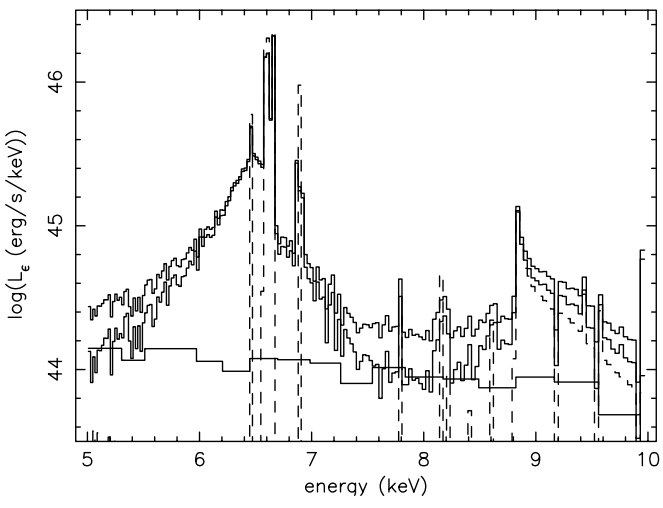

FIG. 4*b*

FIG. 4.—Reflected (*solid curves*) and emitted (*dashed curves*) spectra from nearby models with nonnormal incidence and enhanced iron. Units are specific luminosity, corresponding to the reflected and reprocessed spectrum from gas surrounding a source with ionizing luminosity 10^{47} ergs s^{-1}. Solid curves correspond to Comptonized thermal emission, Compton reflected continuum, and total. (*a*) Model 2″ with $\mu = 0.05$ and Fe = 30 times solar. (*b*) Model 2″ with $\mu = 0.05$ and Fe = 100 times solar.

Fig. 4*a*) and model $2'' \times 100$ (85° and Fe 100 times solar; Fig. 4*b*). A comparison with the similar inclination but solar abundance model $2''$ in Figure 3*b* shows that increasing the iron abundance results in an increase in the line luminosity, both emitted and escaping, by factors that are approximately consistent with the square root scaling described above; model $2'' \times 100$ gives an enhancement in the escaping unscattered luminosity by a factor of 10 over that for solar model $2''$. Compared with a model with normal incidence and solar abundance, model $2'' \times 100$ has an unscattered Fe line luminosity a factor $\gtrsim 270$ times larger ($L_{\rm FeUs} = 5 \times 10^{44}$ ergs s^{-1}), a fractional line luminosity $L_{\rm FeUs}/L_{\rm ref} = 0.02$, and an equivalent width EW = 1.28 keV.

Figure 5 shows the results for two distant cases, model $6'' \times 30$ (85° incidence with Fe 30 times solar, Fig. 5*a*) and model 6×100 (normal incidence with Fe 100 times solar). Comparison of the nearby model $2'' \times 30$ (Fig. 4*a*) and the comparable distant model $6'' \times 30$ (Fig. 5*a*) shows a strong 6.4 keV fluorescence component in the distant model that is not present in the nearby models. The Fe XXVI and Fe XXV components are of comparable strength in the two models. The presence of the fluorescence component is due to penetration of ionizing photons into the partially ionized zone of the distant model. This does not show up in the nearby models because the size of the ionization fronts in photoionized models scale proportional to $\sqrt{Ln}$ (Kallman & McCray 1982; McCray, Wright, & Hatchett 1978), so that in the nearby models fewer photons capable of photoionizing iron penetrate into the partially ionized zone of the model slab. The large incident angle then implies that many of these photons can escape un-Comptonized; the normal incidence distant models produce these photons at greater depths, such that Comptonization smears them as they escape. The unscattered Fe line flux from model $6'' \times 30$ is $L_{\rm FeUs} \sim 2.5 \times 10^{45}$ ergs s^{-1}, a factor of $\sim$5 larger than for model $2'' \times 100$ shown in Figure 4*b*. The fractional line luminosity from this model $6'' \times 30$ is $\sim$0.1, and the equivalent width is 1.03 keV. This is an example of a model in which the continuum near the unscattered line is dominated by the Compton shoulder while the 1–10 keV continuum is dominated by the scattered continuum. The result is that the line-to-continuum ratio is the largest of all the models in Table 1, but the equivalent width is not.

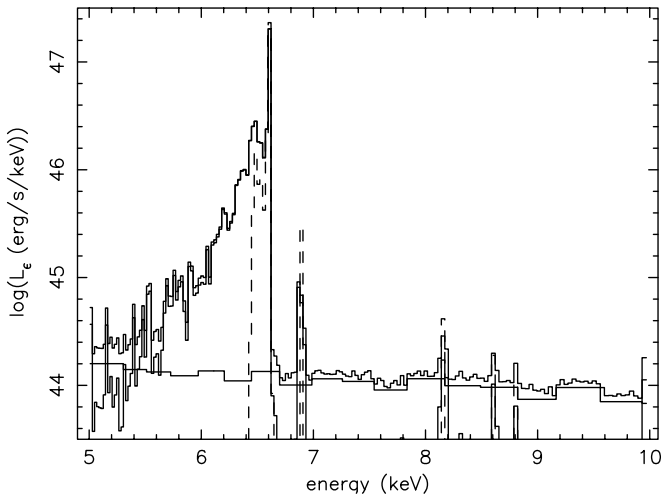

FIG. 5*a*

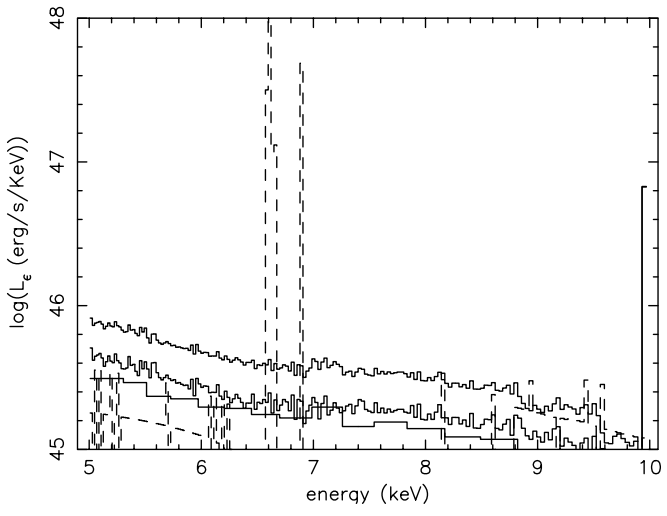

FIG. 5*b*

FIG. 5.—Reflected (*solid curves*) and emitted (*dashed curves*) spectra from distant models with enhanced iron, varying the incidence angle. Units are specific luminosity, corresponding to the reflected and reprocessed spectrum from gas surrounding a source with ionizing luminosity 10^{47} ergs s^{-1}. Solid curves correspond to Comptonized thermal emission, Compton reflected continuum, and total. (*a*) Model $6'' \times 30$, $\mu = 0.05$ with Fe = 30 times solar. (*b*) Model 6×100, normal incidence with Fe = 100 times solar.

The distant models do not show as large line-to-continuum ratios and equivalent widths when low incidence angles are assumed. This is seen in Figure 5*b* for model 6×100, for normal incidence and Fe abundance 100 times solar, giving a line-to-continuum ratio of 0.0015 and an equivalent width of 0.011 keV.

4.5. *Comparison of Model Properties and Dependences*

Comparing Figures 3, 4, and 5, we see that a high inclination increases substantially the escaping unscattered line fluxes, as does increasing the Fe abundance. For similar ionization parameters, chemical abundances, and normal incidence, the distant models appear to produce only marginally larger line fluxes than nearby ones. This approximate parity remains as one increases the chemical abundances. However, for large incidence angles, the distant models appear to produce larger line fluxes than nearby ones, by factors up to $\sim$10, other factors being similar. This is seen in the line-to-continuum ratios and equivalent widths of Table 1. For the same inclination angle and overabundance, the line-to-continuum ratio is a factor of 20 larger in model $6'' \times 30$ than in model $2'' \times 30$. Model $6'' \times 30$ (Fig. 5*a*) gives a line-to-continuum ratio of 0.1, which is also a factor of 5 larger than model $2'' \times 100$ (Fig. 4*b*), which gives 0.02. This reflects the fact that at larger incidence angles the line arises from shallower depths, and the lower densities of the distant models lead to more penetration of the iron-line photons into the partially ionized zone of the slab. The disparity between nearby and distant models is greatly reduced when the line equivalent width is considered. The equivalent width of all the nonnormal incidence models with enhanced iron are comparable to within $\simeq$50%, reflecting the influence of the Compton shoulder on the continuum near the line and variations in the shape of this feature from one model to another.

The absolute values of the line-to-continuum ratio and equivalent widths in the normal incidence case are not only

similar for distant and nearby models but are also much lower for the normal incidence angle cases (Table 1). This is also seen from a comparison of Figure 3*a* (model 2, normal, solar) and Figure 3*b* (model 2″, 85°, solar): the line is much stronger in the inclined case. This is also the case even if one boosts the abundance in the normal incidence case, as in Figure 5*b* (model 6×100, normal, 100 times solar) compared with Figure 5*a* (model $6'' \times 30$, 85°, 30 times solar); even though the latter has lower abundance, its unscattered line is stronger than in the higher abundance, normal incidence case.

We have also examined the effect on our models of reducing the maximum photon energy in the illuminating spectrum from 10 MeV to 100 keV for models $2'' \times 100$ and 6×100. This choice of cutoff is similar to that used by Ballantyne et al. (2001). The ionization parameter, and therefore the incident flux in the 13.6 eV to 13.6 keV band, is the same as in the other versions of models 2 and 6. This has the effect of eliminating pair production and lowering the Compton temperature to 3×10^7 K, which results in increasing the recombination rate and thereby the line luminosities. Since the 13.6 eV to 13.6 keV flux is held constant, the total incident flux is lower in the 100 keV cutoff models, and therefore so is the total energy deposited in the slab. This has the effect of reducing the energy in the emitted line, particularly in the deepest parts of the cloud. The escaping line luminosity is increased by ~20% for model $2'' \times 100$, since in this model much of the line comes from deep in the cloud and the two effects act oppositely. In model 6×100 most of the escaping unscattered line comes from the recombination region, so the 100 keV cutoff model significantly enhances the escaping line.

Interpretation of these results in terms of observations requires the introduction of additional assumptions. Although the most straightforward observational quantity that can be derived from the models is the total line flux emitted by the cloud, observations of the line are affected by Compton broadening of the line and by the statistical significance of the line relative to the adjacent continuum. The line and continuum have differing dependence on reprocessing: the line must be reprocessed, while the continuum may include direct (unreprocessed) radiation. Moreover, we can envision various geometrical configurations for our model reprocessors even within the assumptions of a time-steady unbeamed continuum source. If the reprocessor has a covering fraction relative to the source less than unity, then the observed continuum near the line would likely be dominated by photons from the source. If the photons from the source are not directly observable, either because of time delays or because of beaming away from us, then the observed continuum near the line would be entirely due to Compton reflection and emission from the reprocessor. This simplified continuum scenario is what we consider in Figures 3 and 4. Calculations of the line luminosity presented so far have illustrated the importance of Compton downscattered gamma rays on the spectrum emitted in the cloud interior. Since this process occurs primarily at large depths in the reprocessor, line photons must traverse a corresponding column to escape, and scattering during this process broadens the line. Although we consider these results to be an accurate prediction of the spectra corresponding to our assumed choice of parameters, they are likely to be quite sensitive to our assumptions regarding the reprocessor geometry. Clearly, the assumption of normal incidence onto a plane-parallel slab will produce the lowest fraction of escaping unscattered line photons. Other geometries, such as nonnormal illumination or non–plane-parallel reprocessors, will produce a greater fraction of photons created at large depths that will escape unscattered. Therefore, we consider it likely that real reprocessors will produce lines with luminosities in a range between the unscattered luminosities and the total emitted luminosities (for normal incidence) given in the table.

Our results differ from the calculations of McLaughlin et al. (2002), who considered Comptonization in a funnel geometry, in that the reprocessors considered here have a Compton temperature $\simeq 10^8$ K, so that the mean energy shift per scattering is large. Thus we do not predict easily identifiable spectral features associated with once- or twice-scattered photons, even for photons emitted at small depths. We have not explored different assumptions about the incident continuum shape, which could lead to reduced Compton temperature. We note, however, that it is unlikely that the temperature in the line-emitting region will be low enough (i.e., $\leq 10^6$ K) that the effects of thermal broadening in the Compton escape will be negligible.

Our results shown in Figure 3*b* are similar to those calculated by Ballantyne & Ramirez-Ruiz (2001) in the effects of Comptonization on the lines from H-like and He-like Fe. However, the difference between Figures 3*a* and 3*b* illustrates the dependence of this result on the assumed geometry; at normal incidence the behavior is qualitatively different. Our models differ from those of Ballantyne & Ramirez-Ruiz (2001) in the choice of high-energy cutoff for the illuminating continuum and therefore in the Compton temperature. Our model continua extend to 10 MeV and have a Compton temperature $\simeq 3 \times 10^8$ K. A consequence of this is a lower recombination rate coefficient and correspondingly lower reprocessing efficiency.

4.6. *Pair Production*

Pair production occurs due to γ-γ collisions collisions between incident and reflected photons. We use rate coefficients taken from Coppi & Blandford (1990, eq. [4.6]):

$$R_{\rm prod} \simeq c\sigma_{\rm Th}\left(\frac{F}{c\epsilon_{\rm ave}}\right)^2 f_1 f_2 \ , \tag{6}$$

where $\epsilon_{\rm ave}$ is the average photon energy and f_1 and f_2 are factors less than unity describing the penetration of gamma rays and the albedo for upward photons, respectively. The rate of destruction by annihilation is approximately

$$R_{\rm dest} \simeq \tfrac{3}{8} c\sigma_{\rm Th} n_e n_p \ . \tag{7}$$

Equating these gives an equilibrium pair density relative to protons of

$$\frac{n_e}{n} \simeq \frac{\xi}{c\epsilon_{\rm ave}}\left(\frac{8 f_1 f_2}{3}\right)^{1/2} \tag{8}$$

which is $n_e/n \simeq 10^5 (8 f_1 f_2/3)^{1/2}$ for $\xi = 10^4$, being proportional to ξ. Thus pair production can significantly enhance the total electron number density if the incident spectrum has a significant flux above ~1 MeV and if the reprocessor albedo is not negligible. The effect of pairs on the iron line will be twofold: to enhance the iron recombination rate and thereby the line luminosity, and to decrease the mean free

path of photons to Compton scattering. The Thompson depth in a pair-dominated cloud is proportional to $n_e R \propto \xi n R \propto L/R$, the compactness parameter (e.g., Coppi & Blandford 1990).

In order to evaluate quantitatively the effects of pairs, we have included a calculation of the pair formation rate and of the equilibrium pair density self-consistently in all our models, using the following procedure: In our iterative procedure we initially set the continuum opacity and upward flux of gammas to be zero. As part of the Monte Carlo transfer calculation we calculate the number of pairs produced as a function of depth $N_{\rm pairs}(z)$ and the number of upward photons versus depth and energy, $N_{\rm up}(\epsilon, z)$. Pair production is calculated using the rate coefficient $R(x)$ from Coppi & Blandford (eq. [4.6]) together with the number of upward photons versus depth. The cross section for pair production is given by $\sigma_{\rm pair\,prod} = \max[R(x)F^{(n)}(\epsilon, z)]/c$, the maximum is taken over all upward photon energies, and $F^{(n)}(\epsilon, z)$ is the local upward photon number flux as a function of energy ϵ. The value of $F^{(n)}(\epsilon, z)$ is calculated from the number of upward photons $N_{\rm up}(\epsilon, z)$ by $F^{(n)}(\epsilon, z) = F^{(n)}_{\rm inc} N_{\rm up}(\epsilon, z)/N_{\rm tot}$. This step is repeated a number of times ($\sim$10) to self-consistently calculate the pair production and upward flux of gammas. Pair production is included in the XSTAR calculation by converting the number of pairs created at each depth to a rate by $R_{\rm pair\,prod}(z) = F^{(n)}_{\rm inc} N_{\rm pairs}(z)/N_{\rm tot}$. Destruction (annihilation) is calculated using the rate given in Coppi & Blandford (eq. [3.7]). The equilibrium pair density is added to the ordinary free-electron density and allowed to contribute to recombination, line formation, and so on. This is equivalent to assuming that the pairs thermalize before annihilating. This can be justified by noting that the timescale for slowing down a fast ($\sim$1 MeV) particle in a fully ionized gas is approximately $10^3 n_{12}^{-1}$ s, while the e^+e^- annihilation timescale is longer by a factor of $\sim$a few (Bussard, Ramaty, & Drachman 1979). Both Monte Carlo and photoionization steps are repeated a number of times ($\sim$4) to self-consistently calculate transfer, ionization, pair production/annihilation, and so on. We also implement a self-consistent updating of the optical depth scale when iterating between the XSTAR and Monte Carlo parts of the problem. This is done by performing the Monte Carlo in optical depth space, so the only density-dependent quantity is the ratio of pair cross section to scattering cross section for each flight. The pair production rate is found to converge to within $\simeq$10% after three iterations between the Compton and XSTAR parts of the calculation if the reflected flux is initially assumed to be zero.

The effects of pairs are shown in the table by comparing models 2, 5, and 7 with the corresponding models, which are identical but which have the effects of pairs turned off (models 2np, 5np, and 7np, respectively). At each point in the model the local effect of pairs is to increase the recombination rate and thereby decrease the level of ionization of the gas, increasing the density of ions such as Fe XXVI and Fe XXV. Since the photoionization heating rate increases proportional to these abundances, the effect is to increase the gas temperature. This, in turn, increases the optical depth to photoabsorption by highly ionized iron, thereby reducing the photoionization heating rate deeper in the cloud. Pairs cause the temperature to be greater at small depth and lower at large depth than would otherwise be the case. Since the iron line emissivity is generally a decreasing function of temperature for photoionized models, the two regions will have competing effects on the total line luminosity. The results of the table show that the line luminosity is unchanged by pairs for models 2 and 7 and is slightly decreased by pairs for model 5. This difference between models can be attributed to the greater compactness of model 5 compared with either model 2 or model 7. The unscattered iron-line luminosity is affected more by the neglect of pairs than is the emitted line luminosity, reflecting the fact that pairs affect the optical depth scale more than the temperature distribution. An additional effect of pairs, for reprocessors with densities less than we consider here, is to reduce the Compton mean free path relative to the cloud size. This can allow clouds with low (proton) column densities to be Thomson thick.

5. EFFECTS OF CONTINUUM VARIABILITY AND TIME DELAYS

Most of the results discussed so far are independent of whether the observer sees the radiation from the entire reprocessor at the same time, assuming an illuminating radiation that is constant in time. In reality, the illuminating radiation flux level changes in time, typically being a smoothly decreasing function of time. For the nearby-reprocessor models 1–5, the finite light-travel time differences between different parts of the reprocessor are negligible for observer times $t_{\rm obs} \gtrsim 10^2$–10^3 s, particularly if the radiation arises from a limited range of solid angles, such as a funnel. However, for the distant-reprocessor models 6–7, the finite light-travel time between the continuum source and the shell means that the observer sees simultaneously different parts of the reprocessor, which are illuminated by the continuum at different source times. The regions nearest to the observers are illuminated by a continuum corresponding to later source times than the regions farther from the observer. This convolution can be described by an equation of the form

$$L(t) = \frac{f}{2}\int_{\theta_{\rm min}}^{1} \sin\theta\, d\theta \int_0^t dt'\, L_{\rm line}(\theta, t')\delta \times \left(t - t' - R\frac{1-\cos\theta}{c}\right) = \frac{f}{2}\frac{c}{R}\int_{\max(1, t-2R/c)}^{t} dt' L_{\rm line}\left\{\cos^{-1}\left[1 - \frac{c}{R}(t-t')\right], t'\right\},$$

where $L_{\rm line}(\theta, t)$ is the emitted luminosity from the surface of the reprocessor as a function of observing angle and time, f is a factor of $\leq$1 that takes into account the fact that the reprocessor can be clumpy (as seen by the source it can cover less than 4π), and the line emission is not isotropic. The integral is over the surface of the reprocessing shell illuminated by the continuum, which may be beamed (e.g., Weth, et al. 2000). For distant models the effect of time delays have been considered also by Lazzati et al. (1999) and Böttcher (2000) and in a torus geometry by Böttcher & Fryer (2001). The main effect is that the peak line (or reprocessed continuum) luminosity is smaller than the line fluxes given in Table 1, because of smearing by integration over the surface. For the simplest case, where the ionization is dominated by the initial hard pulse of duration $t_{\rm illum}$ observed at a later time $t_{\rm obs}$, this would give a dilution factor of the order $t_{\rm illum}/t_{\rm obs}$ that could be $\lesssim 10^{-1}$ to 10^{-2}, where $t_{\rm obs} \sim (2R/c)(1 - \sin\theta_j) \sim$ day, depending on the model. In

such models (e.g., model 7 of Table 1) the line luminosity actually observed would be diluted below the value of $\sim 10^{46}$ ergs s^{-1} given in the table by an amount which could be substantial, depending on the luminosity evolution. For instance, if the continuum luminosity $L_{in} \sim 3L_X$ of model 7 ($L_{in} = 10^{52}$ ergs s^{-1}, which could not last longer than tens of seconds) evolves on a timescale of a day to a value comparable to that of model 6 ($L_{in} = 10^{47}$ ergs s^{-1}), and if this spectrum still illuminates the shell of gas (i.e., at 1 day the afterglow shock producing the continuum has not outrun the shell, which requires exceptional densities inside the shell; e.g., Weth et al. 2000), then the line luminosity would be at least the value $10^{44.5}$ given for model 6. A quantitative discussion of the Fe light curves is affected by uncertainties in the model details that would require geometrical and parameter space investigations beyond the purposes of this paper. However, detailed calculations of specific models (Weth et al. 2000; Böttcher 2000; Böttcher & Fryer 2001, etc.) agree with the above approximate estimate of $L_{Fe} \lesssim 10^{43}$–10^{44} ergs s^{-1} if solar abundances are used in a distant reprocessor scenario.

6. ILLUMINATION AND ABUNDANCE EFFECTS

For the distant models the results are dependent on the illumination model. If the jet producing the input radiation remains within the reprocessor shell after 1–1.5 days (requiring rather high intrashell densities) and continues to illuminate the reprocessor material as the luminosity evolves down to $L_{in} = 10^{47} \sim 3L_X$ ergs s^{-1} in model 6, then 30 times solar abundances are sufficient. However, if the afterglow shock or jet producing the illuminating continuum outruns the reprocessor shell in less than a day, then the effective continuum is a prompt flash of duration much less than a day with a luminosity comparable to model 7, but the line intensities of model 7 would be affected by a dilution factor of 10^{-2} to 10^{-3} because of the time-delay smearing discussed in the previous section and larger increases in the solar abundance relative to solar may be needed.

Relevant to the abundance issue, e.g., in the distant reprocessor scenarios if these are associated with recent supernova events (e.g., Piro et al. 2000; Vietri et al. 2001; Reeves et al. 2002), is the production of adequate amounts of iron via the decay of nickel and cobalt, involving a delay of order 70 days. If the supernova occurred less than a few months before the GRB, then the shell may contain supersolar nickel but not much iron. In nearby models, if supersolar abundances are required, highly nickel-enriched material may be entrained by the jet from the core to the outer edges of the funnel in the envelope. In the nearby models, the case has been made that multiple Compton scatterings in the stellar funnel (McLaughlin et al. 2002) will cause the nickel line energies to mimic those of iron. In the distant models, multiple scatterings are not expected, so the necessity for producing iron is harder to avoid. In our models, we can crudely test for the effects of having nickel instead of iron by modifying the abundances in the model scenario that most nearly resembles the supernova reprocessor. We have done this in model 6ni, in which we have used the conditions for model 6, but have set the iron abundance to 0 and instead chosen a nickel abundance such that the number density of nickel ions is the same as the number density of iron ions in model 6. This corresponds to a 20 times overabundance of nickel relative to the solar values of Grevesse, Noels, & Sauval (1996). (Owing to uncertainties in atomic data, XSTAR does not include cobalt, so we cannot directly test scenarios involving mixtures of this element.) The results are given in Table 1, in which the line strengths in the "Fe" column for model 6ni correspond to nickel rather than iron. We find that the dominant nickel line is the helium-like complex at 7.78 keV, and the strength of this feature in model 6ni somewhat exceeds the strength of the Fe XXVI line in model 6. This feature appears prominently in the model spectrum and would lead to a greater inferred redshift for the source if it were the true origin of the feature observed in, e.g., GRB 991216.

7. DISCUSSION

The results of the previous sections indicate that iron-line luminosities in the range of $\sim 10^{43}$–$10^{45.5}$ ergs s^{-1}, comparable to the luminosities observed so far (e.g., Piro et al. 2000), can be produced by photoionization of a dense reprocessing gas in the vicinity of gamma-ray burst sources. The model densities and ionization parameters assumed in both "nearby" scenarios (e.g., the jet plus bubble model of Mészáros & Rees 2001 or the delayed jet model of Rees & Mészáros 2000) and in "distant" scenarios (e.g., the preexisting supernova shell of Lazzati et al. 1999; Piro et al. 2000; Vietri et al. 2001) are generally able to do this, with higher line luminosities achieved if one uses Fe abundances $\sim$30–100 times solar and/or large incidence angles $\theta_i \gtrsim 80°$. However, the models so far are highly simplified, and while they address particular aspects, they are not yet at the stage where they can provide a general fit to all the properties of particular afterglows where X-ray lines have been reported. This is partly due to the small and sparse set of line observations, whose significance level is not high, and to the complex nature of the models, which involve a number of poorly constrained parameters.

An Fe-group metal overabundance relative to solar is plausible both in nearby models, where the stellar progenitor funnel walls can be enriched by the jet or bubble bringing up enriched core material, and in the distant model, where a preexisting supernova shell would also consist of core-enriched material. However, in both nearby and distant models (in the latter if the shell age is less than $\sim$70 days), the heavy ions may be mainly Ni instead of Fe. In nearby models there is a plausible way of degrading Ni lines to resemble Fe lines through multiple scattering (McLaughlin et al. 2002), while in distant supernova (SN) shell models a somewhat older shell or some other mechanism for making Ni appear as Fe is required.

Another important parameter in photoionization models of line formation is the incidence angle at which the input continuum reaches the reprocessing gas. This, at least for the simple models considered here, is subject to some natural constraints. For nearby models involving a funnel in a stellar envelope illuminated by a jet or bubble, a large incidence angle is quite plausible. On the other hand for distant models, such as a supernova shell ejected days or months before the burst, the radiation is unlikely to reach the shell at a large incidence angle. Even if the shell is lumpy, the incidence angle would be expected to be closer to normal.

A significant observational constraint on the models is the line to continuum ratio (Lazzati, Ramirez-Ruiz, & Rees 2002; Ghisellini et al. 2002). A nominal "target" value is given by the *Chandra* observations of GRB 991216 (Piro

et al. 2000), for which an equivalent width EW = 0.5 ± 0.013 keV is quoted in discussing the observer-frame spectrum.

The observer-frame energy equivalent width is related to the source-frame value by $EW_{ob} = EW_{em} 1/(1+z)$, and the object is at $z \sim 1$, so the GRB 991216 source frame EW ~ 1 keV is the quantity to be compared against our source frame calculations. In Table 1 we have defined the line-to-continuum ratio on the basis of the continuum in the 1–10 keV range; hence using $E_{max} = 10$ keV, $E_{min} = 1$ keV, and a canonical -1 spectrum, the relation is

$$EW = (F_{line}/F_{cont}) E_{line} \ln(E_{max}/E_{min}) \quad \text{or}$$
$$(F_{line}/F_{cont})_{GRB991216} = (EW/E_{line})/\ln(E_{max}/E_{min}) \sim 0.06 .$$

This measure of line reprocessing efficiency depends on the continuum measured over a wide energy range, and in the objects with line detections so far many of these photons are redshifted out of the observable energy band.

Table 1 shows that the models that approach the GRB 991216 comparison value for the line continuum ratio of 0.06 (or -1.2 in log scale) are model $2'' \times 100$ (nearby, 87° incidence angle, 100 times solar), which has a line-to-continuum ratio of $\sim$0.02, and model $6'' \times 30$ (distant, 87° incidence angle, 30 times solar), which has a line-to-continuum ratio of $\sim$0.1. The GRB 991216 comparison value for the line equivalent width of 1 keV (in the source frame) is achieved or surpassed by $2'' \times 30$, $2'' \times 100$, $6''$, and $6'' \times 30$. Equivalent width is a measure of reprocessing efficiency that depends on the continuum in the immediate vicinity of the line. The equivalent widths that we calculate approach or exceed 0.5 keV for the nearby and distant models that include both nonnormal incidence and an iron overabundance.

For the same high incidence angle and a lower overabundance, the distant model makes a stronger line than the nearby model. This has been explained in § 4.5 in terms of the shallower line depths in high incidence angle cases, with the lower density of distant models leading to more penetration of Fe line photons.

However, the line-to-continuum model values of Table 1 were calculated in the spirit of investigating how the physics of the line production varies as a function of the basic model parameters. In particular, the abundances and the incidence angles were varied more or less arbitrarily, and this needs to be supplemented with astrophysical considerations of how plausible particular parameter values are in the context of given models.

In distant scenarios, a large Fe overabundance is reasonable if there is a weeks to months delay between the supernaova and GRB explosions, requiring good timing so that enough Fe has been formed but the shell has neither dispersed nor is too close. In nearby scenarios, a large Fe-group overabundance is also plausible, as matter is dredged up from the core by the jet. Furthermore, multiply downscattered Ni lines, as they bounce in the funnel, can mimic the Fe lines (McLaughlin et al. 2002). This possibility of Ni-mimicking Fe does not work in distant scenarios, where multiple scattering are not expected. Another aspect of multiple reflections in a stellar funnel is that it can increase somewhat further the line-to-continuum ratio (Ghisellini et al. 2002). Other possible difficulties have been pointed out for nearby models, e.g., Ghisellini et al. 2002, which were based on analytical calculations for normal incidence conditions.

A large incidence angle is naturally expected in nearby models, from the geometry of a funnel in a stellar envelope. An example of this is the nearby model $2'' \times 100$ with 87° incidence angle and 100 times solar Fe, which has a line-to-continuum ratio of 0.02 and an equivalent width of 1.28 keV. On the other hand, a large incidence angle is less likely in a distant supernova shell model, where quasi-normal incidence is the natural expectation. A normal incidence distant model such as 6×100, even with 100 times solar Fe, produces a line-to-continuum ratio of 0.001 and an equivalent width of 0.011 keV (Table 1 and Fig. 5*b*). Other models, in general, have lower values.

Both nearby and distant models, in their simple versions as discussed here and elsewhere, are constrained by total energetics (Ghisellini et al. 2002; Kumar & Narayan 2003), and these issues were not addressed here. As far as the ability of these models to reproduce the observed nominal 0.06 line-to-continuum ratios or 1 keV equivalent widths, values approaching this can be achieved in distant (supernova) models if a large incidence angle is used, which for this model appears implausible. Values within a factor of 3 of this can be achieved with nearby (stellar funnel) models, using optimistic but plausible parameters. The line-detection significance in this object is 4.5 σ for Kα and K-edge identification or 3.5 σ for the Kα alone (Piro et al. 2000). Given the 3–4 σ confidence level in the existence of the lines and the line-to-continuum ratios and equivalent widths, as well as the highly approximate nature of the models, it may be too early to reach strong conclusions about preferring one model over another.

The exact shape of the line and the fraction escaping in a narrow core are sensitive to the geometry and other model details of the reprocessor. For this reason, we have not attempted here to make a detailed comparison of models to specific observations but rather concentrate on the more general question of the effect on observable quantities of various physical properties inherent in the two main generic classes of models that have been recently discussed. In the two scenarios, the line is computed on the basis of the continua listed in Table 1. For the nearby scenarios, we can assume that the continuum observed is $\gtrsim$ the continuum exciting the observed lines. As emphasized by Lazzati et al. (2002), this is an upper limit, since a fraction of the continuum may reach the observer directly. The X-ray lines are generally seen accompanied by a bump-like rise in the X-ray continuum, which in the nearby scenario is attributed to a rising bubble or a secondary late-jet component producing its own X-ray power law, which interacts with the outer stellar envelope (Rees & Mészáros 2000; Mészáros & Rees 2001). The line timescale of 1–2 days is caused by the intrinsic timescale of the (subrelativistic) bubble rise or secondary long-term jet, and relativistic or geometrical time delays are negligible since the illumination timescale is comparable to the observation time. This component is somewhat in excess of that attributed to the canonical relativistic main jet, which is thought to produce the GRB at early times, and which at $t \gtrsim 1$ day, when its Lorentz factor has dropped to values of $\sim$10 at radii $\gtrsim 10^{16}$ cm, is thought to give rise to the standard power law (but not to X-ray lines) seen in canonical X-ray afterglows.

In distant reprocessor scenarios involving, e.g., invoking a supernova shell (Lazzati et al. 1999; Vietri et al. 2001; Piro et al. 2000; Weth et al. 2000; Böttcher 2000; Böttcher & Fryer 2001; Ballantyne & Ramirez-Ruiz 2001), the

photoionizing continuum is assumed to be due to the same canonical jet responsible for the GRB. The shell distance in this model is determined from geometrical considerations [time delay $\sim(R/c)(1-\cos\theta_{\rm sh})\sim 1$–2 days, where $\theta_{\rm sh}$ is shell effective angle]. For such distant models, unless the density inside the shell exceeds $\sim 10^6$–10^7 cm^{-3} the jet producing the X-ray continuum would have moved beyond the shell at $t\sim 1$ day, and hence the appropriate photoionizing luminosity is that at early times while the jet is inside (e.g., model 7); the line luminosities in Table 1 for model 7 have to be multiplied by a time-delay dilution factor that would be $\sim t_{\rm ill}/t_{\rm obs}\lesssim 10^{-1}$ to 10^{-2} , and this might make the line-to-continuum ratio lower than observed. More detailed time delays have been discussed in the literature cited, using, however, specific model geometries, which is not our purpose here. On the other hand, within the spirit of our approximate geometry models, the distant model 6 (in particular the 30 times times solar Fe model 6×30) at high incidence angles has an input luminosity corresponding to a time delay factor $t_{\rm ill}/t_{\rm obs}\lesssim 1$ and leads to line–to–X-ray continuum ratios in the observed range. Two additional assumptions involved in distant scenarios are (1) that line-producing ejecta shell has had months to decay from Ni into Fe, requiring a supernova to have occurred months before the burst, for which stellar evolutionary scenarios are currently very speculative, and (2) that the shell at $R\sim 10^{16}$ cm of total mass of $\sim$few solar masses is either geometrically very thin, $\Delta R/R\lesssim 10^{-3}$, or else consists of very dense blobs whose density happens to provide a covering factor of order unity.

The recent reports of *XMM* observations of Mg, Si, and S lines, but no Fe lines, from GRB 011211 (Reeves et al. 2002) and from GRB 020813 (Butler et al. 2003), which appeared months after submission of this paper, is in strong contrast to the five previous GRB line detections referred to elsewhere in this paper (e.g., Piro et al. 2000, etc.). If this interpretation is correct, it would imply different conditions in this burst compared with the previous five bursts that showed Fe lines. For example, in photoionized models, this might arise from a different ionizing spectrum, ionization parameter, or illumination history, and so on. (Lazzati et al. 2002). We note that the collisional ionization mechanism favored by Reeves et al. (2002) would imply very high densities for an SN shell (10^{15} cm^{-3}), and such densities would be more naturally expected in nearby reprocessor scenarios, in addition to conditions that could lead to mixed collisional ionization and photoionization.

Further diagnostic information about the reprocessor is available from detections or limits on absorption features due to bound-bound or bound-free transitions of iron. For the physical conditions envisaged in this paper, photoionization equilibrium is a good approximation and nonequilibrium effects are expected to be small. With different model assumptions, however, these might play a role, e.g., possibly in enhancing the radiation recombination (free-bound) edge (Yonetoku et al. 2001; Yoshida et al. 2001) or in producing an absorbing column that varies with time after the initial burst onset (Lazzati, Perna, & Ghisellini 2001; Lazzati & Perna 2002). Enhanced recombination may occur if the electron temperature is (very) low compared with the ionization temperature, which is less likely under photoionization conditions but may be possible if the gas undergoes sudden rarefaction and adiabatic cooling of the electrons. The data on GRB 991216 that they discuss is close to what is predicted by the simple photoionization equilibrium models discussed here. In general, the bound-free absorption cross section from the K shell of iron is not a sensitive function of the ionization state of iron, and it is comparable with the Thomson cross section if the abundances are cosmic and the ionization is favorable. Since all the reprocessors described in the previous section are effectively semi-infinite, they will not transmit efficiently near iron, so absorption features (e.g., as reported, at the $3\,\sigma$ level, by Amati et al. 2000) are not expected from these simplified models. Absorption features would be imprinted on the reflected continuum from thick reprocessors at ionization parameters lower than those we examine here, e.g., $\log(\xi)\leq 100$, but this does not appear to be compatible with conditions inferred from observed emission lines. However, if the Thomson depth of the reprocessor were, at least temporarily, close to unity (as might be expected in a nearby reprocessor model, as the jet and the prompt portion of its relativistic waste bubble breaks through the last few optical depths at increasing angles), such features may also be naturally expected.

In conclusion, we have investigated both nearby and distant models of GRB afterglow reprocessor geometries proposed as sources for the reported X-ray lines in several GRBs, through photoionization by an incident continuum. We find that the effects of Comptonization and pair formation can affect the results, depending on the conditions assumed. The absolute values of the line luminosities can be reproduced fairly well by both models if high overabundances and high incidence angles are assumed. While distant (e.g., SN shell) models are more effective at producing high line-to-continuum ratios and equivalent widths at high incidence angles, such angles are not expected to occur naturally without some further assumptions being introduced, and at quasi-normal incidence the line ratios are too low. Nearby reprocessors (e.g., stellar funnel) can account naturally for high incidence angles and reach line-to-continuum ratios and equivalent widths within a factor of 3 of the reported values. Issues remain concerning overall agreement with the entire burst history as well as energetics. Further line observations at higher significance levels, as well as more detailed modeling, will be required before strong conclusions can be reached concerning the type of progenitors and geometries involved.

We are grateful to Xin-Min Hua for use of the Comptonization code, to D. Ballantyne, E. Ramirez-Ruiz, and D. Lazzati for discussions, and to NASA NAG 5-9192 and the Royal Society for support.

REFERENCES

Amati, L., et al. 2000, Science, 290, 953
Ballantyne, D., & Ramirez-Ruiz, E. 2001, ApJ, 559, L83
Ballantyne, D., Ross, R., & Fabian, A. 2001, MNRAS, 327, 10
Bautista, M., & Kallman, T. 2001, ApJS, 134, 139
Böttcher, M. 2000, ApJ, 539, 102
Böttcher, M., & Fryer, C. 2001, ApJ, 547, 338
Bussard, R., Ramaty, R., & Drachman, R. 1979, ApJ, 228, 928
Butler, R. N., et al. 2003, ApJ, submitted (astro-ph/0303539)
Coppi, P., & Blandford, R. 1990, MNRAS, 245, 453
Ghisellini, G., Lazzati, D., Rossi, E., & Rees, M. J. 2002, A&A, 389, L33
Grevesse, N., Noels, A., & Sauval, A. 1996, in ASP Conf. Ser. 99, Cosmic Abundances, ed. S. Holt & G. Sonneborn (San Francisco: ASP), 117

Guilbert, P. 1986, MNRAS, 218, 171
Hua, X. 1997, J. Comp. Phys., 11, 660
Kallman, T., & Bautista, M. 2001, ApJS, 133, 221
Kallman, T., & McCray, R. 1982, ApJS, 50, 26
Krolik, J., McKee, C., & Tarter, C. B. 1981, ApJ, 249, 422
Kumar, P., & Narayan, R. 2003, ApJ, 584, 895
Lazzati, D., & Perna, R. 2002, MNRAS, 330, 383
Lazzati, D., Perna, R., & Ghisellini, G. 2001, MNRAS, 325, L19
Lazzati, D., Ramirez-Ruiz, E., & Rees, M. J. 2002, ApJ, 572, L57
Lazzati, D., et al. 1999, MNRAS, 304, L31
McCray, R., Wright, C., & Hatchett, S. 1977, ApJ, 211, L29
McLaughlin, G. C., Wijers, R., Brown, G., & Bethe, H. 2002, ApJ, 567, 454
Mészáros, P., & Rees, M. 2001, ApJ, 556, L37
Morrison, R., & McCammon, D. 1983, ApJ, 270, 119
Nayakshin, S., et al. 2000, ApJ, 537, 833
Piro, L., et al. 1999, ApJ, 514, L73
———. 2000, Science, 290, 955
Rees, M. J., & Mészáros, P. 2000, ApJ, 545, L73
Reeves, J. N., et al. 2002, Nature, 416, 512
Tarter, C. B., Tucker, W., & Salpeter, E. 1969, ApJ, 156, 943
van Paradijs, J., Kouveliotou, C., & Wijers, R. A. M. J. 2000, ARA&A, 38, 379
Vietri, M., Ghisellini, G., Lazzati, D., Fiore, F., & Stella, A. 2001, ApJ, 550, L43
Weth, C., et al. 2000, ApJ, 534, 581
Yonetoku, D., et al. 2001, ApJ, 557, L23
Yoshida, A., et al. 1999, A&A, 138, 433
———. 2001, ApJ, 557, L27